Current Medical Imaging, 2022, *18*, 939-951

RESEARCH ARTICLE

Microwave 3D Imaging System Featuring the Phase Coherence Factor for Improved Beamforming

Rasammal Rasappan[1], Nik Syarim Nik Anwar[2], Tareq Faisal Zanoon[3], Tiang Sew Sun[4], Mohd. Fadzil Ain[1] and Mohd. Zaid Abdullah[1,*]

[1]*School of Electrical and Electronic Engineering, Engineering Campus, Universiti Sains Malaysia, 14300 Nibong Tebal, Pulau Pinang, Malaysia;* [2]*Faculty of Electrical Engineering, Centre for Robotics & Industrial Automation, University Teknikal Malaysia 76100 Durian Tunggal, Melaka, Malaysia;* [3]*Faculty of Engineering and Information Technology, Computer Systems Engineering Dept. Arab American University P.O Box 240 Jenin, Palestine;* [4]*Faculty of Engineering, Technology & Built Environment, Electrical and Electronic Engineering Department, UCSI University, Cheras, 56000 Kuala Lumpur Campus, Malaysia*

Abstract: ***Background*:** This paper presents an improved radar-based imaging system for breast cancer detection that features p-slot ultrawideband antennae in a 32-array set-up. The improved reconstruction algorithm incorporates the phase coherence factor (PCF) into the conventional delay and sum (DAS) beamforming algorithm, thus effectively suppressing noise arising from the side- and grating-lobe interferences.

***Methods*:** The system is tested by using several breast models fabricated from chemical mixtures formulated on the basis of realistic human tissues. Each model is placed in a hemispherical breast radome that was fabricated from polylactide material and surrounded by 32 p-slot antennae mounted in four concentric layers. These antennae are connected to an 8.5 GHz vector network analyser through two 16-channel multiplexers that automatically switch different combinations of transmitter and receiver pairs in a sequential manner.

***Results*:** The system can accurately detect 5 mm tumours in a complex and homogeneously dense 3D breast model with an average signal-to-clutter ratio and full-width half-maximum of 7.0 dB and 2.3 mm, respectively. These values are more competitive than the values of other beamforming algorithms, even with contrasts as low as 1:2.

***Conclusion*:** The proposed PCF-weighted DAS is the best-performing algorithm amongst the tested beamforming techniques. This research paves the way for a clinical trial involving human subjects. Our laboratory is planning such a trial as part of future work.

ARTICLE HISTORY

Received: September 14, 2021
Revised: December 20, 2021
Accepted: December 28, 2021

DOI:
10.2174/1573405618666220304093447

Keywords: Breast cancer detection, ultrawideband, phase coherence factor, beamforming, delay and sum, side-lobe noise.

1. INTRODUCTION

Amongst all cancer fatalities, those due to breast cancer can be avoided if this malignancy can be detected early [1]. Recent studies have shown that the survival rate of patients with early-stage breast cancer has increased from 93% to 100% [2]. Hence, the regular screening and health check-ups of people in the high-risk category are crucial for detecting cancerous cells in the early stage of development. Mammography remains one of the popular methods for breast cancer screening [3,4]. Nevertheless, one principal drawback of mammography is related to the use of X-ray radiation, which may cause serious health issues in patients, especially those undergoing repeated screening [5]. Furthermore, its lower detection rate of tumours in dense tense than in fatty breast tissue has led to high false positives in the reported cases [6,7]. Magnetic resonant imaging (MRI) is another popular tool, particularly for women with dense breast tissue. However, MRI requires lengthy examination procedures and complicated image analysis steps that include interpretation. Above all, this technique requires a very expensive instrument and is usually performed in major hospitals for detailed assessment or, in some cases, as a tool for diagnostic confirmation [8]. Ultrasound is another device that is useful for lesion detection. Similar to mammography, ultrasonic radiography can distinguish between fluid-filled cysts and solid tumours. However, it is very operator dependent and needs special skills for system operation.

Microwave imaging in the ultrawideband (UWB) range has recently emerged as a promising technique for breast

*Address correspondence to this author at the School of Electrical and Electronic Engineering, Engineering Campus, Universiti Sains Malaysia, 14300 Nibong Tebal, Pulau Pinang, Malaysia; Email: mza@usm.my

1875-6603/22 $65.00+.00

cancer detection due to its nonionising properties and safety factors [9,10]. This technique works by transmitting high-frequency low-power impulses (GHz range) into the breast and measuring the corresponding scattered energy along different directions. The scattered fields are then used to reconstruct an image that depicts the profile of the scatterer in 2D or 3D by taking measurements from different planes. The passive, active, and hybrid methods are three different methods for performing microwave imaging measurements [11]. Confocal microwave imaging techniques are branches of active microwave imaging wherein beamforming is an integral process in image reconstruction [11-18]. Beamforming methods can be classified into two different categories. The data-adaptive method [12,13] constitutes the first category, and the data-independent method [14,15] falls under the second category. Each method has its own strengths and drawbacks. For example, data-independent beamformers are less complex than data-adaptive beamformers and are hence fast algorithms. By contrast, the data-adaptive method is very time-consuming even though it enables considerably more accurate reconstruction than the data-independent method. For both cases, in general, the quality of image reconstruction improves as the number of measurements increases. However, this situation presents some challenges to hardware and software designs. The fabrication of lightweight probes, the management of huge numbers of sensors, and the processing of an enormous amount of data within a very short period are some common problems associated with hardware. Meanwhile, runtime increases almost exponentially as the number of measurements is increased. Hence, a complex-designed software solution is needed to achieve runtime with a reasonable speed.

Numerous image reconstruction techniques have been studied and developed to improve runtime while maintaining accuracy at acceptable levels. Amongst these techniques, the data-independent delay and sum (DAS) method, which is also one of the earliest beamforming methods developed for microwave-imaging applications, is popular. It is also widely used for the quantitative mapping of the dielectric property of a region of interest in multistatic configuration [14, 16]. Simplicity, fast runtime, and high amenability to parallel computation are some of the attractive features of DAS over other considerably more complex beamformers. Thus, this work focused on the DAS beamforming algorithm and its derivatives, such as CF, DMAS, and EDAS. As evident from the literature, traditional DAS is a very popular algorithm with numerous researchers in the field [17, 18]. However, although DAS can detect malignancy quite effectively, it produces images that are noisy and cluttered mainly because its undersampling behaviour limits its capability to reconstruct an image accurately. Overcoming this problem has led to the development of another version of DAS, which is referred to in the literature as the delay, multiply and sum (DMAS) algorithm [19]. Essentially, DMAS works by firstly multiplying every signal pair measured from the same transmitter with each other and then summing and squaring the results. In this way, the number of samples is increased, thereby improving the overall sensitivity of the algorithm to the scatterer and reducing clutter. In another approach, a weighting function is introduced to further minimise cluttering and improve overall image quality [20]. For example, the incorporation of a coherent factor (CF), which is defined as the ratio between the coherent and incoherent sums of the received signals, into DAS [21] resulted in a significant reduction in cluttering as suggested by the results of previous researchers. Similarly, applying the same procedure to DMAS resulted in another variant of DAS, namely, the enhanced delay and sum (EDAS) algorithm. Previous results have indicated that EDAS provides highly accurate reconstruction with average signal-to-clutter ratio (SCR) and signal-to-mean ratios of 5 and 10 dB, respectively [22]. These figures correspond to an increase in image accuracy of more than 140%, reflecting the efficiency of CF in reducing clutter. However, this technique is effective only in suppressing clutter caused by side-lobe interference. Hence, the image remains blurry and contains a large amount of noise, especially when measurements are attempted with wide-element-spacing phased array antennae wherein interferences are dominated by grating lobes [23]. Consequently, a clutter-suppression technique with increased robustness and power is needed to address these types of artefacts. One solution is to exploit the phase diversity of the interfering signals through the use of the phase coherence factor (PCF); such an approach is a very popular technique in ultrasonic imaging applications [24]. In contrast to CF, PCF is not only effective in suppressing noise caused by side-lobe interferences but also those originating from grating lobes as proven by ultrasonic experiments.

In this work, we investigate the application of PCF to reduce clutter and improve image-to-noise ratios in 3D UWB measurements. The proposed approach is tested experimentally by using a set-up comprising 32 p-slot antennae mounted onto a hemispherical phantom mimicking the ordinary glandular type of an adult female breast. The performance of the proposed algorithm is evaluated in terms of accuracy, SCR, and speed.

2. PROPOSED METHOD

The basic working principle of microwave imaging technology is based on an incident wave from a transmitter travelling through a breast and its interactions with tumours or other muscular tissues in the breast. Scattering is caused when this wave encounters inhomogeneities along its travelling paths. The scattered fields are then measured by several receivers placed around the breast. The proposed method relies on multistatic configurations [25] where N distributed transceiver antennae are used. Measurements are performed by transmitting UWB signals through one antenna, while the scattered signals on all other antennae are measured sequentially. This process is repeated until all antennae have been used for transmission. Hence, $N(N-1)$ measurements are available from the N-antenna geometry.

Prior to image reconstruction, the system is calibrated by performing measurements with the homogeneous phantom to simulate the healthy or tumour-free breast. This approach produces one set of signals containing scattered fields, namely, $s_{p,m,n}(t)^{healthy}$, where m, n, and t represent the transmitter, receiver, and sampling time, respectively. Then,

the same measurements are repeated on the cancerous breast phantom to produce another set of scattered fields, namely, $s_{p,m,n}(t)^{cancerous}$. Subtracting the first set from the second set yields $s_{p,m,n}(t)$, which contains calibrated signals for all different (m,n) combinations and for each sampling time. Mathematically,

$$s_{p,m,n}(t) = s_{p,m,n}(t)^{cancerous} - s_{p,m,n}(t)^{healthy} \quad (1)$$

In this way, the systematic errors due to variances in antenna characteristics, cables, multiplexer channels, and multipath reflections are minimised. In a real application, $s_{p,m,n}(t)^{healthy}$ can be produced by making measurements on several healthy subjects and averaging the results.

The image reconstruction algorithm is explained in Fig. (**1**), which shows one $m - n^{th}$ pair positioned on the surface of the target and separated by the distance *d.* In this case, the *m*-th transmitter Tx generates the UWB impulse that travels in the object and encounters the ideal scatterer p located at the focal point (x_p, y_p, z_p) before being reflected back to the *n*-th receiver Rx. The backscattered signal from the focal point *p,* i.e. $s_{p,m,n}(t)$, can be modelled as the delayed version of the transmitted signal envelope, A(.) *i.e.*

$$s_{p,m,n}(t) = A\left(t - \tau_{p,m,n}\right) \quad (2)$$

where $\tau_{p,m,n}$ is the total propagation delay in the medium from the m^{th} transmitter to the focal point p and back to the n^{th} receiver. The total delay time is calculated as follows:

$$\tau_{p,m,n} = \frac{r^{total}}{v} \quad (3)$$

where r^{total} is the total distance travelled by a scattered signal from the m^{th} transmitter to the focal point p and back to the n^{th} receiver and v is the velocity of propagation. In this equation, r^{total} is expressed as:

$$r^{total} = r_{1,p} + r_{2,p} \quad (4)$$

where $r_{1,P}$ and $r_{2,P}$ are computed by using the Euclidean distances between the m^{th} and n^{th} transceivers. The velocity v can be calculated from the given relative permittivity of the homogeneous background material ε_r and the speed of light c.

Similar to that in other image reconstruction algorithms, in this case, sampling as many signals as possible is preferred to reduce noise and improve reconstruction quality. This preference thus involves mounting as many sensors as possible onto a target and making measurements from as many projections as possible. This approach is impossible to implement because the size of the sensor is usually comparable with that of an object. Moreover, increasing the number of sensors would result in a reduction in the spacing element d as shown in Fig. (**1**). Theoretically, d must be equal to or less than half of the wavelength to fulfil the Nyquist sampling criterion. Otherwise, radiation perfor-

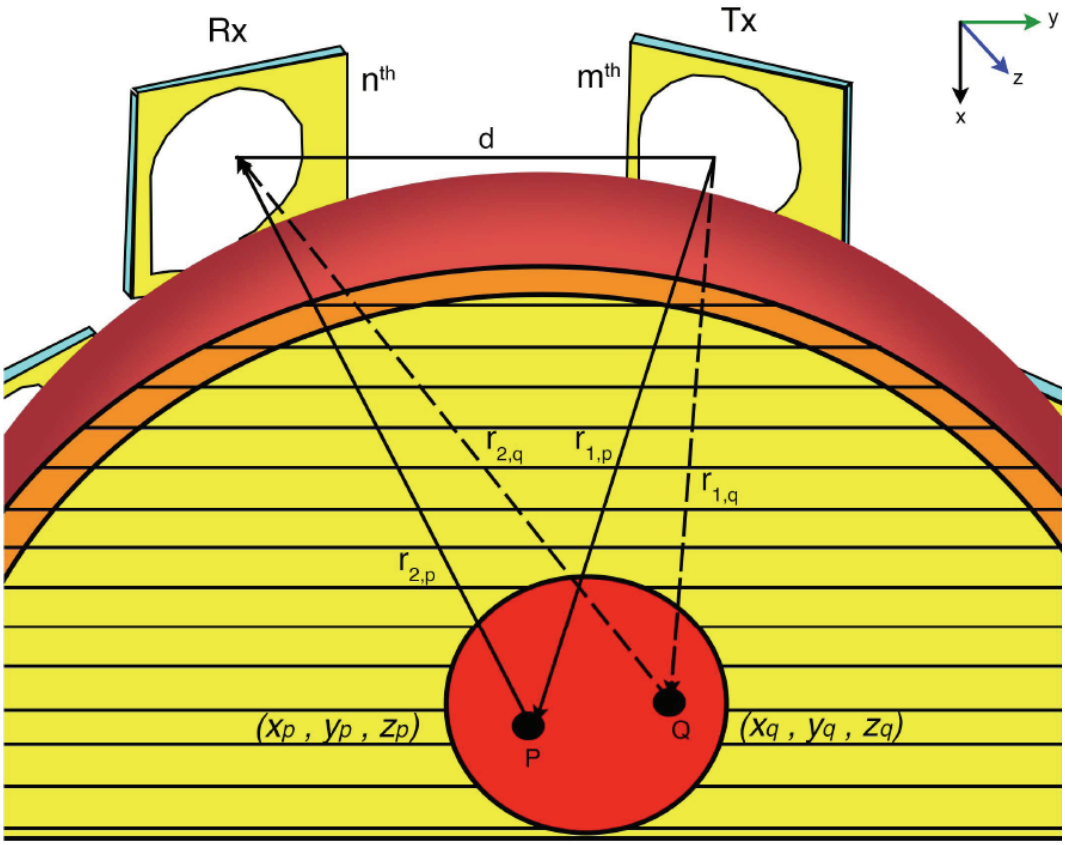

Fig. (1). The geometry of propagation delay in a heterogeneous medium. (*A higher resolution / colour version of this figure is available in the electronic copy of the article*).

mance deteriorates due to the formation of grating and side lobes [26]. In most cases, d is usually based on the lowest operating frequency. Such a situation is acceptable for narrow-band systems but poses a challenge to UWB systems due to the narrowing of the main lobe and the widening of side or grating lobes with the increase in frequency [27, 28]. Given the presence of these interfering lobes, the reflection from other scatterers, particularly those located in proximity to the focal point as represented by point q in Fig. (**1**), are detected. Consequently, $s_{p,m,n}(t)$ is out of focus. Hence, Eq. (2) needs to be modified by incorporating the difference in the delay time between the intended and other focal points. Mathematically,

$$s_{q,m,n}(t) = A\left(t - \tau_{p,m,n} + \Delta\tau_{m,n}\right) \quad (\mathbf{5})$$

where $\Delta\tau_{m,n}$ is the difference in the propagation delay for each transceiver pair between the intended focal point p and nearby scattering point q. The measured signal $s_{q,m,n}(t)$ can be refocused to the intended focal point p by shifting the signals by $\tau_{p,m,n}$, resulting in:

$$s'_{q,m,n}(t) = A\left(t + \Delta\tau_{m,n}\right) \quad (\mathbf{6})$$

where $s'_{q,m,n}(t)$ represents the time-shifted signal.

If the scatterer q is located at the focal point p, then all the received signals have equal time delays and are exactly in phase, i.e., $\Delta\tau_{m,n} = 0$. By contrast, if q is out of focus and lies in different side lobes, then $\Delta\tau_{m,n} \neq 0$ and varies with *m–n* across the aperture. The out-of-focus signal can be assessed on the basis of the instantaneous phase $\varphi_{m,n}$ of the delayed signal as described by Eq. (7). An adaptive weighting factor using the statistical analysis of the instantaneous phase $\varphi_{m,n}$ is applied to detect the signal that lies outside the main lobes. In this approach, all received signals are weighted by PCF, which is defined on the basis of the standard deviation of the instantaneous phase $\varphi_{m,n}$ [29]. In this case, the $\varphi_{m,n}$ of the echo signal (6) is calculated by using the Hilbert transform defined as [30]:

$$\varphi_{m,n} = tan^{-1}\left(\frac{H\{s'_{q,m,n}(t)\}}{s'_{q,m,n}(t)}\right) \quad (\mathbf{7})$$

where $H(\cdot)$ represents the Hilbert transform.

Similar to the other variables expressed in the inverse tangent trigonometric function, the instantaneous phase is within the range of [–π to +π] [31]. Consequently, the uncertainty in phase variance is increased. Obtaining the instantaneous phase by using a complex function is the best way to overcome this uncertainty. In so doing, Eq. 6 is firstly expressed in complex form, and the time is then eliminated to yield:

$$\sigma(e^{j\varphi_{m,n}}) = \sqrt{\sigma^2\left[\cos\left(\varphi_{m,n}\right)\right] + \sigma^2\left[\sin\left(\varphi_{m,n}\right)\right]} \quad (\mathbf{8})$$

where σ^2 denotes the variance of the complex exponential signal. *PCF* can be calculated by using Eqs. (7 and 8). Mathematically,

$$PCF = [1 - \sigma(-j\varphi_{m,n})]^2 \quad (\mathbf{9})$$

Theoretically, the *PCF* that was calculated with Eq. (9) enables the backscattered signals from location p to align such that all start from the same reference point. In other words, they have the same focus point or are in phase. They have the same time delay time in special cases or at an ideal focusing point at which all backscattered signals are in phase. As a result, σ is zero, and hence $PCF = 1$. In this case, no correction is needed, and the system operates as a conventional DAS. By contrast, the phase variation and *PCF* decrease when the signals are out of focus or when they arrive at different times. Correction is needed here to enhance the suppression of the side and grating lobes by multiplying *PCF*, thus yielding:

$$I_p(t) = \int_0^W \left[\sum_{m=1}^{M}\sum_{n=1}^{N} S_N^M\left(t - \Delta_{N,p}^M\right).PCF\right]^2 dt \quad (\mathbf{10})$$

Here, M and N denote the total number of transmitters and receivers, respectively. The corrected output is then squared and integrated over the time window *W*, thus providing the energy value at the focus point $I_{(p)}$. The flowchart summarising the overall procedures of the proposed DAS-weighted PCF is provided in Fig. (**2**).

3. MATERIALS AND METHODS

3.1. Breast Phantom

Considering that cancerous cells are located mainly in the upper outer and lower inner quadrants of the breast [32], we decided to perform experiments with tumours in these two locations. The breast phantom used in the experiments is depicted in Fig. (**3**). In this case, the two cancerous cells are assumed to both have diameters of 5 mm and two different contrast ratios: the first one is 1:5, and second one is 1:2. Here, the two tumours are referred to as Tumours 1 and 2. The above contrast ratios were chosen to test the capability of UWB to detect low- and high-contrast dielectric inhomogeneity. The model shown in Fig. (**3**) was constructed by using chemical materials that were formulated on the basis of the relative permittivity and conductivity of realistic human tissues over the frequency of interest [33]. These chemicals were mixed and moulded into a 90 mm hemisphere. The phantom has a 2 mm skin layer ($\varepsilon_r = 38, \sigma = 2\ \mathrm{sm}^{-1}$), two 20 mm circular glandular structures ($\varepsilon_r = 32, \sigma = 2.9\frac{S}{m}$) with one 5 mm tumour ($\varepsilon_t = 54, \sigma = 2.5\frac{S}{m}$) and a second 5 mm tumour constructed of clay ($\varepsilon_r \approx 20$) embedded within fatty tissue ($\varepsilon_r = 15, \sigma = 0.4\frac{S}{m}$) as illustrated in Fig. (**3a**). In the (x, y, z) coordinate system and as shown in Fig. (**3b**), Tumours 1 and 2 are located at approximately $(80,\ 50,\ 1.27)$ mm and $(70, 90, 31.8)$ mm, respectively. These coordinates were measured from the base or pectoral fascia location of the breast. This area corresponds to the flat sheet of the connective tissue of an ordinary adult woman.

3.1.1. Sensor Array

A compact UWB p-slot antenna was chosen as the array element. This antenna has a wide bandwidth, high coupling efficiency, and a very compact design [24]. An example of

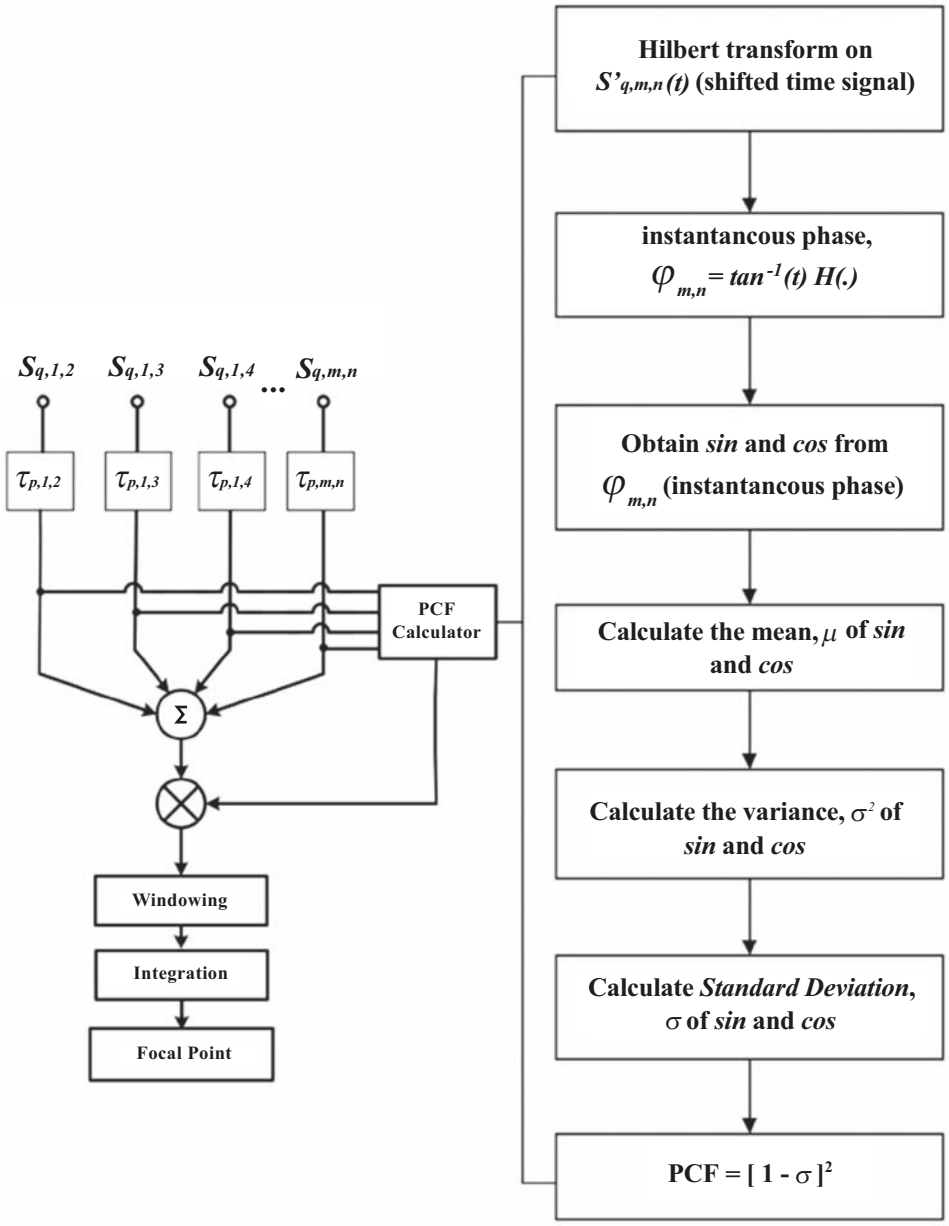

Fig. (2). Flowchart summarizing the proposed PCF-weighted DAS algorithm.

this antenna fabricated by using the substrate Roger RT6010 ($\varepsilon_r = 10.2$) with a thickness of 1.27 mm is shown in Fig. (**4a**). The microstrip feeder was designed on the substrate with a size of 16 mm ×16 mm, as shown in Fig. (**4b**), and a substrate thickness of 1.27 mm. This design exhibits the wideband characteristic defined at the −10 dB threshold and an operation frequency ranging from $4.56 - 11.1$ GHz. Furthermore, this antenna provides significant advantages in terms of size and timing characteristic in different media and delivers a short pulse from the transmitter to the receiver. The normalised correlation factor of this antenna measured in a homogeneous medium is greater than 0.5 at a distance of 120 mm with a transmission coefficient of −40 dB in a heterogeneous set-up. These characteristics make this type of antenna appropriately acceptable for application in breast detection.

3.1.2. 3D Radome

The breast radiation dome or radome used in this study was designed with a hemispherical form to fit the 3D antenna array arrangement. The clinical testing of the patients was considered in the design for future experiments. In this case, the size of a radome has to be sufficiently large to accommodate the 32 p-shaped antennae described previously. The radome was designed with SOLIDWORKS software and printed in 3D by using polylactide material. The radome comprises three important components: the base, antenna holders, and breast holder. Fig. (**5a-c**) shows the prototype. The base was designed from four separate quarters and joined together to obtain a solid foundation for antenna holders. Meanwhile, the antenna holder was arranged in four concentric hemispherical layers with diameters of 90, 70, 50 and 28 mm. Eight antennae are placed equidistantly in each

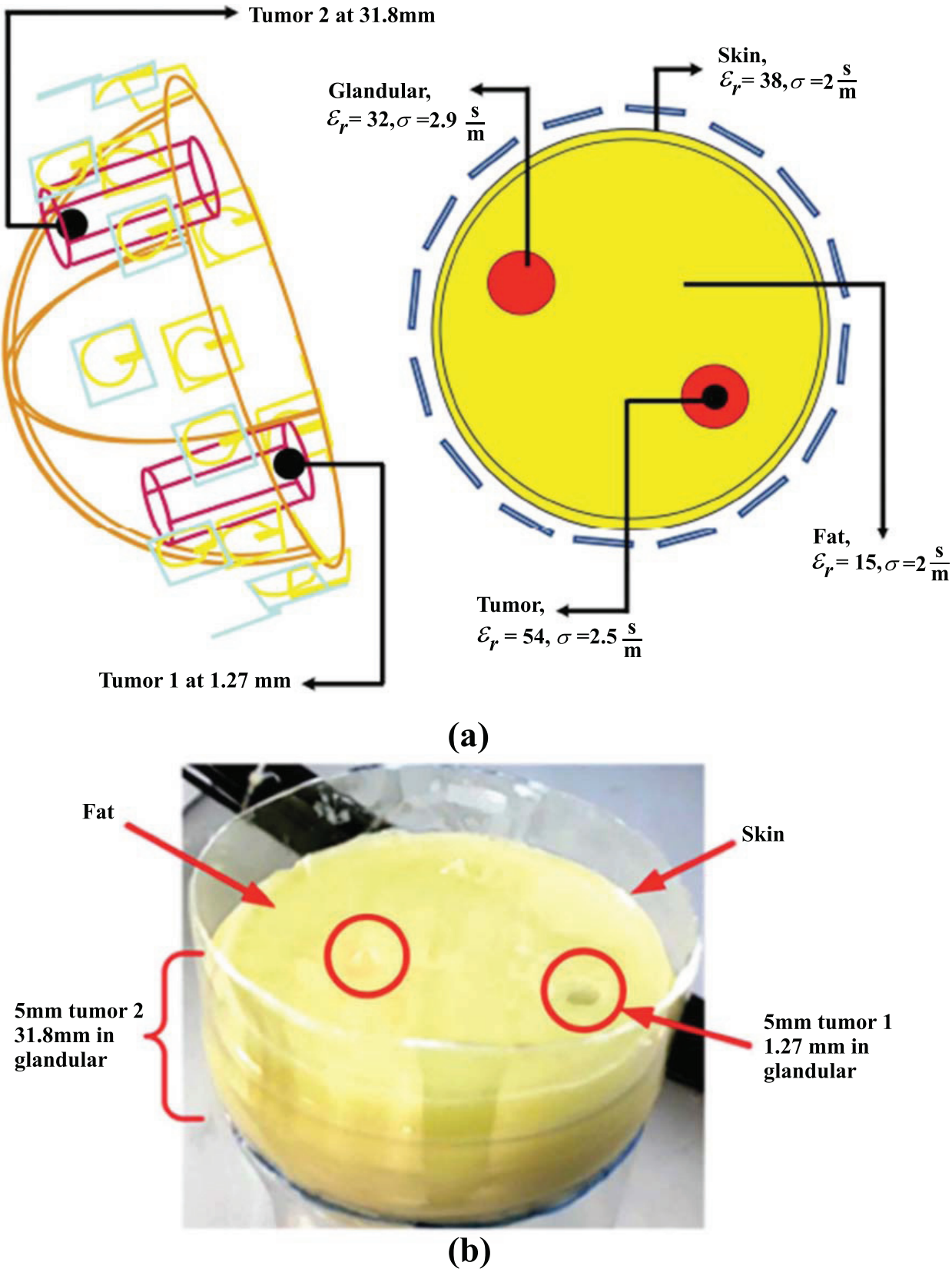

Fig. (3). Heterogeneous breast phantom: (**a**) computer model and (**b**) actual model fabricated from chemical mixtures formulated on the basis of realistic human tissues. (*A higher resolution / colour version of this figure is available in the electronic copy of the article*).

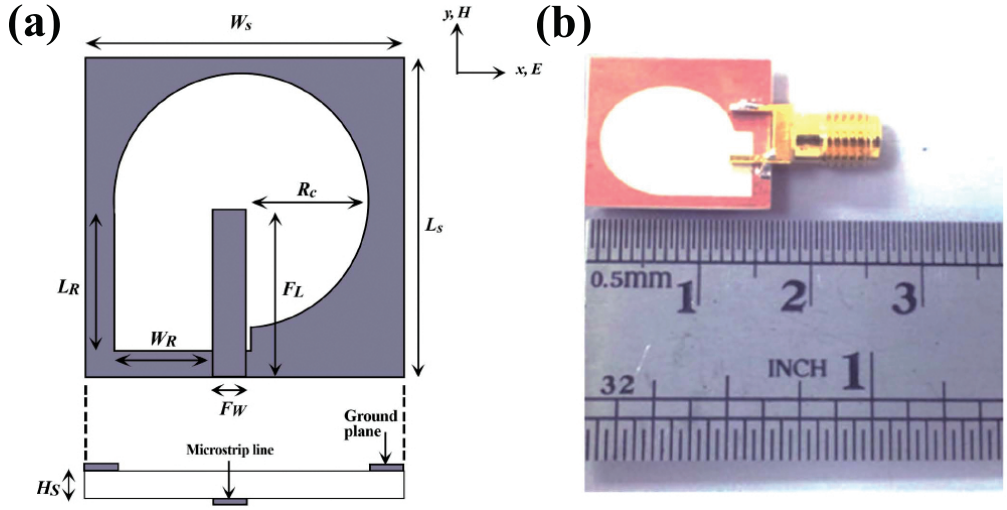

Fig. (4). (**a**) Geometry and (**b**) actual design [26] of the p-shaped wide-slot antenna [34]. (*A higher resolution / colour version of this figure is available in the electronic copy of the article*).

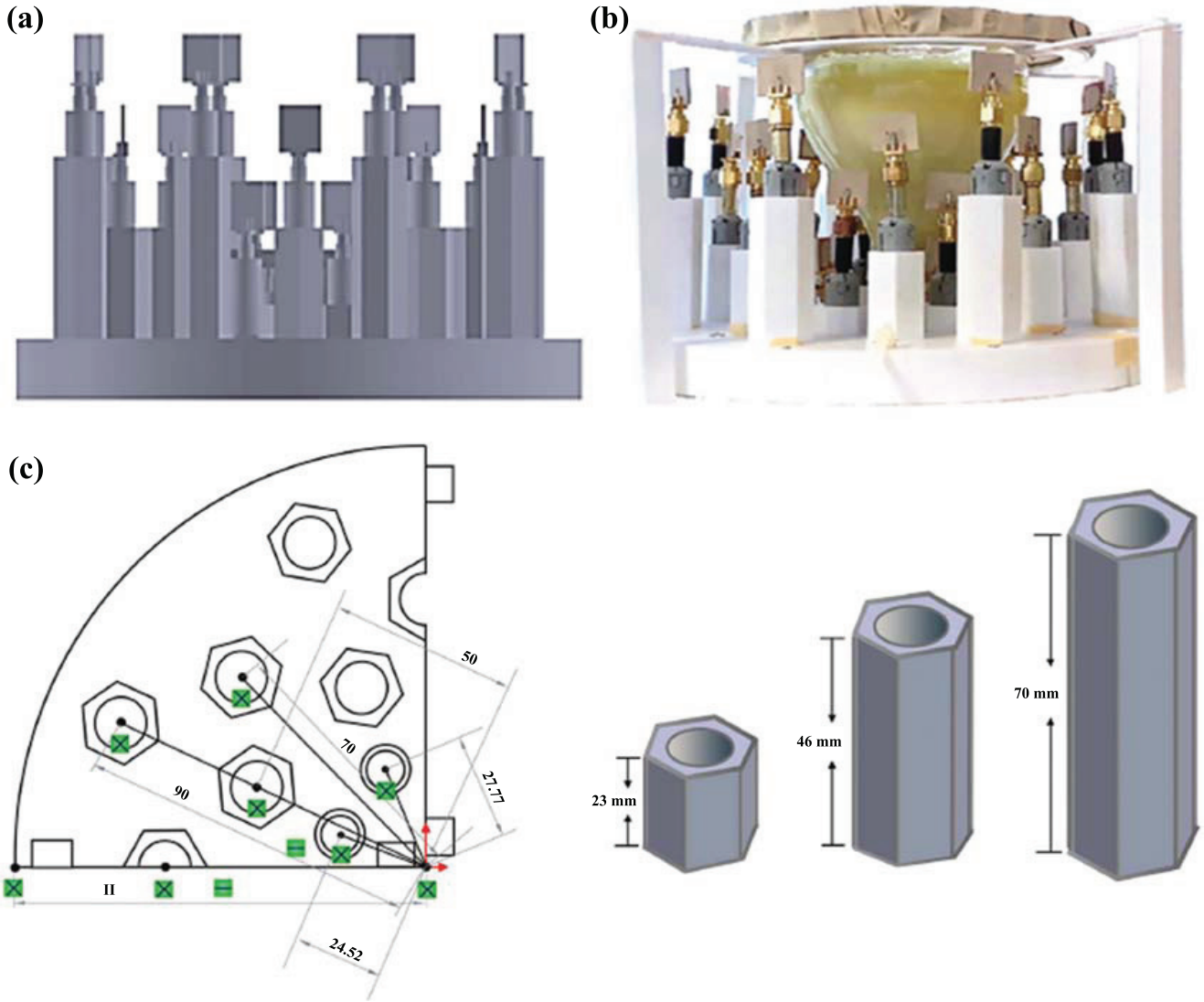

Fig. (5). (**a**) Side view, (**b**) actual set-up of the radome design, and (**c**) three-antenna holders corresponding to three different planes. (*A higher resolution / colour version of this figure is available in the electronic copy of the article*).

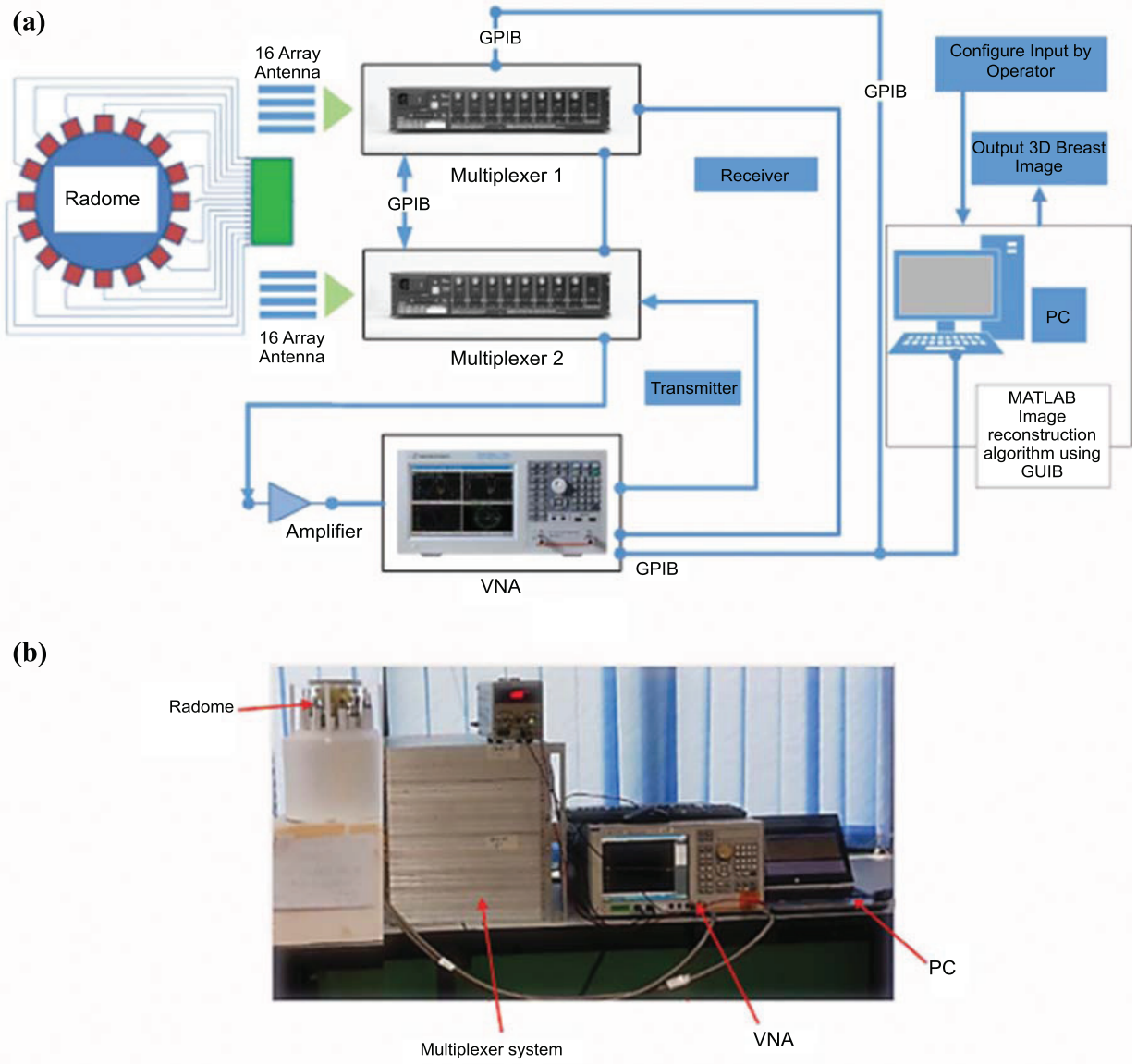

Fig. (6). UWB experimental facilities depicting (**a**) the block diagram of DAS and (**b**) the actual set-up. (*A higher resolution / colour version of this figure is available in the electronic copy of the article*).

layer. Heights were fixed at 0, 23, 46, and 70 mm in correspondence with the antennae located in the first, second, third, and fourth layers, respectively, as illustrated in Fig. (**5c**). As depicted in Fig. (**5b**), the main function of the breast holder is to hold the breast in free space in the prone position. In this way, the signals were transmitted to the breast, reflected, and received by the antennae directly, thus minimising noise due to multipath interferences and other artefacts.

3.1.3. Data Acquisition System

The data acquisition system consisted of two Cytec CXM 16-channel multiplexers that automatically switched different combinations of transmitter and receiver pairs in a sequential manner. The system was connected to an Agilent E5071C 8.5 GHz vector network analyser with a time-domain transformation feature. A 20 dB wideband amplifier was applied to amplify the measured signals. Meanwhile, a general-purpose interface bus was used to control and interconnect all equipment in the bus, allowing the measurements to be performed automatically. The schematic of the data acquisition system is provided in Fig. (**6a**). Fig. (**6b**) shows the actual hardware. Altogether, 992 measurements were acquired from the system, with each measurement containing 201 discretised time-domain data samples. A frequency sweep of 1–6 GHz was used throughout the measurements with a fixed scanning time of 20 ms for each measurement. The measured data were used to perform image reconstruction with standard algorithms, such as DAS, CF, DMAS, and EDAS, serving as references to PCF-weighted DAS as previously described.

4. RESULTS AND DISCUSSION

Reconstructed images were compared in terms of the following parameters to validate the capability of the proposed method in comparison with other approaches: (i)

SCR, (ii) full-width half-maximum (FWHM), and (iii) runtime. In this case, the SCR is a highly convenient approach for assessing an algorithm in the absence of a reference or ground truth image. This quality index is usually used when the regions belonging to the target and clutter appear distinctly. The SCR is calculated as follows:

$$SCR(x,y,z) = 20\log_{10}\left[\frac{\left(\max\left|En_{target}(x,y,z)\right)\right)}{\left(\max\ |En_{clutter}(x,y,z)\right)}\right] \quad (\mathbf{11})$$

where En_{target} is the maximum intensity at a given location (x,y,z), and $En_{clutter}$ is the maximum clutter intensity at a given location (x,y,z) in the same image.

Meanwhile, the spatial resolution of the reconstructed image can be expressed as the FWHM of the point spread function (PSF) [35]. The FWHM is a measure of the physical intensity of a tumour and is calculated as follows:

$$\text{FWHM} = \sigma * \sqrt{8\ln 2} \sim 2.355 * \sigma \quad (\mathbf{12})$$

where σ is the standard deviation of the PSF.

This parameter expresses the normalised intensity distribution of reconstructed images. PSF broadening and hence image blurring can be assessed by using the FWHM. In this case, a low FWHM indicates good image quality. Similarly, a high FWHM indicates noisy and cluttered images. The cluttering is the result of the spillover of a signal from one pixel to its neighbours.

Finally, the practical feasibility of such an imaging system is measured in terms of runtime. A short runtime is indicative of fast reconstruction speed and high system practicality.

4.1. Image Reconstruction

The reconstructed images for the comparison of different algorithms are depicted in 2D and 3D views, as shown in Fig. (**7**). In this case, Figs. (**7a**-**d**) show images that were reconstructed by using standard DAS, CF, DMAS, and EDAS, respectively. The results from the same algorithms incorporated with PCF are shown in Figs. (**7e**-**h**) in the same order. Fig. (**7a**) shows typical images of Tumours 1 and 2 in different locations reconstructed by using standard DAS. As clearly shown by this figure, although the conventional DAS can detect both tumours, the images appear blurry due to the presence of cluttering. Consequently, this algorithm cannot map the exact locations of either tumour accurately. Meanwhile, CF produces a slight improvement in image quality as can be seen from the result in Fig. (**7b**). The image appears slightly more focused even though the reconstruction remains blurry. Hence, mapping the exact location of both tumours, particularly that of Tumour 1, which has a low permittivity contrast ratio, remains difficult. DMAS and EDAS also provided blurry images, as evidenced by Figs. (**7c** and **d**), respectively. By contrast, the blurriness is significantly reduced after the integration of PCF into all algorithms, as suggested by the results in Figs. (**7e**-**h**). As clearly inferred from these results, the tumour images reconstructed with PCF are much more focused than those reconstructed without PCF. The close examination of these figures reveals that DAS outperforms other algorithms, as indicated by the result in Fig. (**7d**). Clearly, this image is considerably cleaner and contains less noise than the images reconstructed by other algorithms. In general, the geometrical properties of a tumour, such as size, shape, and location, can be mapped accurately from the images reconstructed by using PCF.

Table **1** presents a quantitative comparison of the performances of all the algorithms in terms of SCR, FWHM, and runtime. In this case, the SCR and FWHM were calculated and averaged from two tumour locations. Again, as can be seen from this table, the images reconstructed with PCF are generally much better in terms of the SCR and FWHM than those reconstructed without PCF. These results reveal that, on average, the PCF-weighted DAS records the highest SCR of 7.0 dB, and the PCF-weighted EDAS, DMA, and CF have SCR values of 6.1, 5.9, and 3.7 dB. The same trend is repeated in terms of the FWHM. The PCF-weighted DAS presents an FWHM of 2.3 mm, which is the lowest. Given this result, the PCF-weighted DAS is the best-performing algorithm. The second-best algorithm is the PCF-weighted EDAS, which has an average FWHM of 2.5 mm, followed by the PCF-weighted DMAS, which has an FWHM of 2.8 mm. CF demonstrates no significant improvement before and after the application of PCF. The FWHM of this algorithm is 3.8 mm before PCF. This value decreases marginally to 3.3 mm after PCF. These trends can be visualised in terms of the PSF of each reconstruction method plotted in Fig. (**8**). As can be seen from Figs. (**8a**-**d**), for all algorithms, pulse broadening is clearly more prominent before the application of PCF than before. As illustrated in Fig. (**8d**), the effect of PCF is the narrowing of PSF with DAS registering the highest bandwidth reduction of 51% compared with the bandwidth reductions of 38%, 31%, and 23% for EDAS, DMAS, and CF, respectively. The small bandwidth reduction, particularly the reduction shown by DMAS and CF, is likely due to the amplification of noise because the number of measurements increases as a result of data extrapolation instead of increasing the number of viewing angles or sensors. These results also suggest that PCF has benefited DAS significantly in terms of sidelobe suppression while maintaining main lobe resolution. Hence, as suggested by the experimental results, the artefacts can be reduced not necessarily by data extrapolation but by using an appropriate coherence factor with high noise suppression capabilities.

In terms of runtime and with the exception of DMAS, the PCF-weighted algorithms are considerably slower than those without PCF. The increase in time is due to the additional processing required for calculating the PCF coefficients. Amongst the PCF-weighted algorithms, the fastest is DAS with a runtime of 46.8 s, whereas EDAS is the slowest with a runtime of 383 s. The performances of CF and DMAS lie between these two extremes, with the former and the latter recording runtimes of 74 and 378 s, respectively. In contrast to that, in the combination of unique and extrapolated measurements in other algorithms, particularly EDAS and DMAS, only unique measurements are utilised in DAS for image reconstruction. Hence, DAS requires less CPU time than other algorithms. In general, the PCF-weighted DAS is not only the fastest but also the best-performing algorithm.

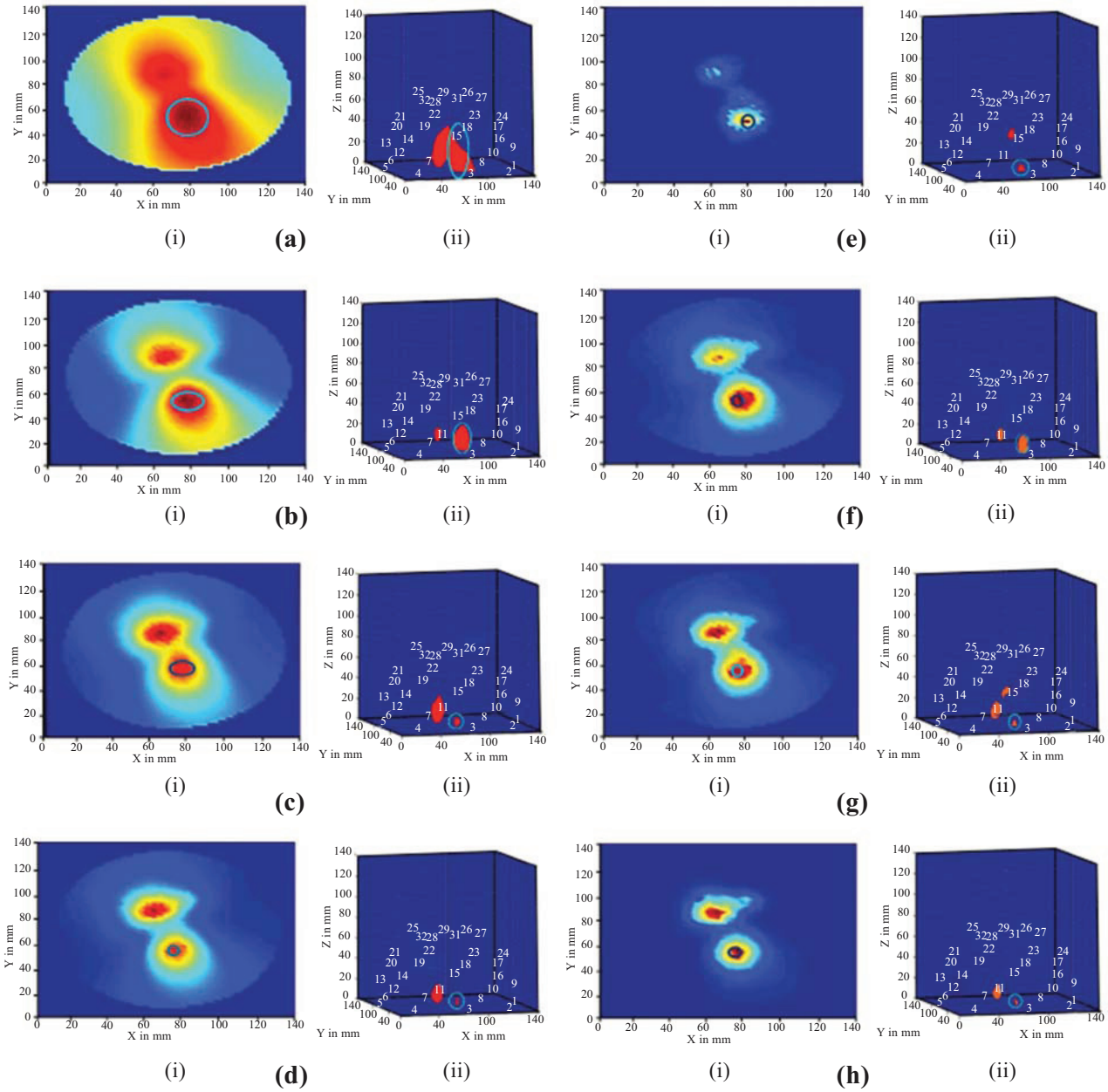

Fig. (7). Reconstructed images comparing the performance of different algorithms. Here (**a**), (**b**), (**c**), and (**d**) are images reconstructed by using standard DAS, CF, DMAS, and EDAS, respectively, whereas (**e**), (**f**), (**g**), and (**h**) correspond to images reconstructed by the same algorithm integrated with PCF. For each method, (i) and (ii) depict images in 2D and 3D, respectively. Tumours 1 and 2 are located in the bottom-right and top-left of each image, respectively. (*A higher resolution / colour version of this figure is available in the electronic copy of the article*).

Table 1. Comparison of common beamforming algorithms in terms of SCR, FWHM, and runtime before and after the application of PCF.

Algorithm	SCR (dB)	FWHM (mm)	Runtime (s)
DAS	1.4	4.7	26
CF	2.8	3.8	27
DMAS	1.8	3.1	331
EDAS	3.8	2.9	336
DAS + PCF	7.0	2.3	47
CF + PCF	3.7	3.3	74
DMAS + PCF	5.9	2.8	378
EDAS + PCF	6.1	2.5	383

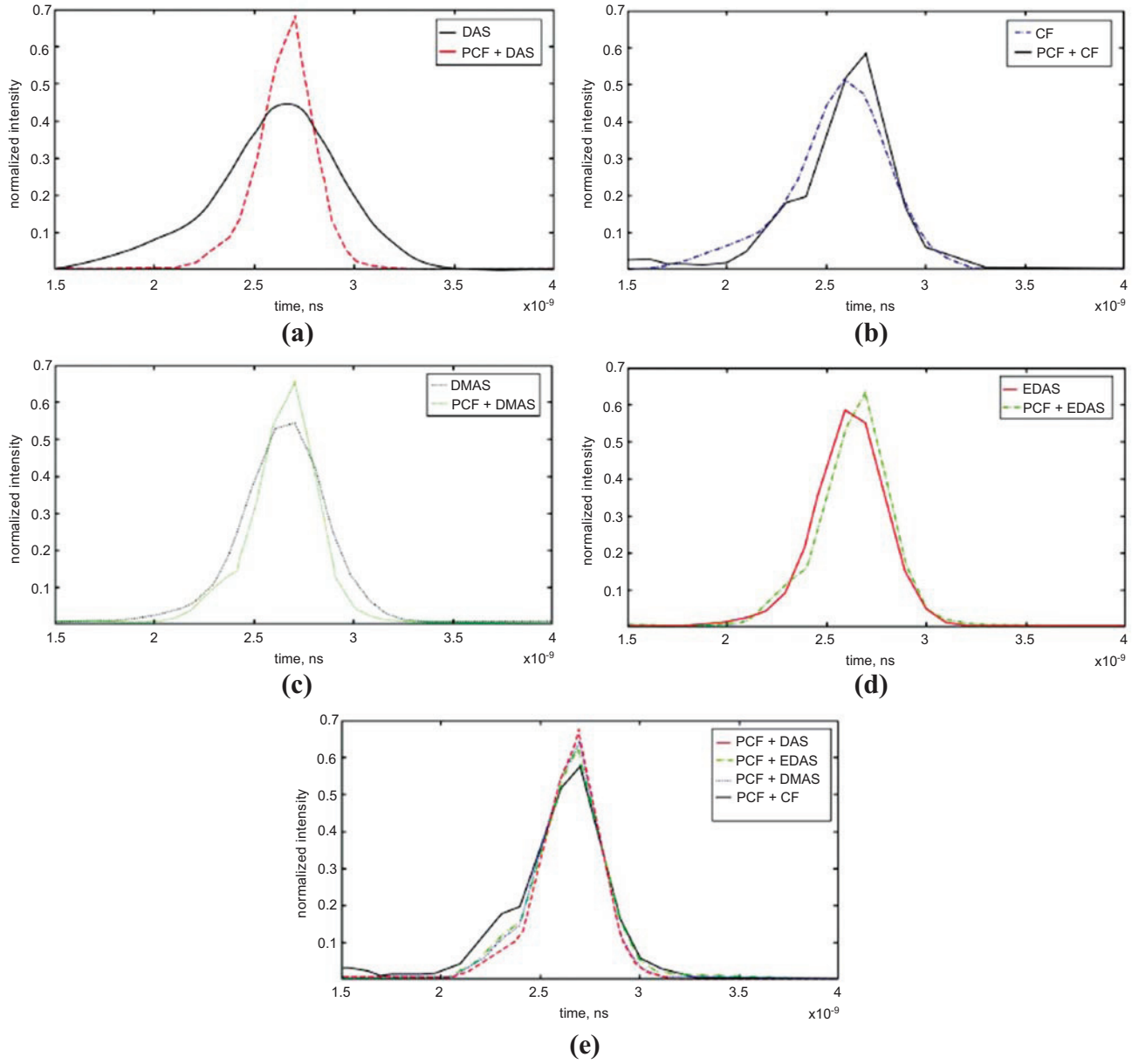

Fig. (8). Comparison of PSF calculated from each beamformer before and after PCF weighting. (**a**), (**b**), (**c**), and (**d**) are the PSF plots produced by DAS, CF, DMAS, and EDAS, respectively, and (**e**) is a comparison of the PSF patterns after the weighting of all algorithms with PCF. (*A higher resolution / colour version of this figure is available in the electronic copy of the article*).

CONCLUSION

An improved DAS beamforming algorithm weighted with PCF is discussed. This algorithm is based on the existing DAS beamforming algorithm but incorporates PCF filtering and the phase estimation method. The additional filter enables the algorithm to achieve considerably enhanced spatial focus, resulting in the reduction in clutter caused by the side- and grating-lobe interferences. The algorithm can accurately detect 5 mm tumours in a complex and homogeneously dense 3D breast model with average SCR and FWHM values of 7.0 dB and 2.3 mm, respectively, which are more competitive than the SCR and FWHM values of other beamforming algorithms even when the contrast between the tumour and the background materials is as low as 1:2. Further proof for the noise-suppressing capability of the improved algorithm is provided by PSF measurements, in which the proposed method, compared with other techniques, narrowed pulses by as much as 30%. Given these results and together with the result showing that it is also the fastest algorithm, the proposed PCF-weighted DAS is the best performing algorithm amongst the beamforming techniques investigated in this study. This research paves the way for a clinical trial involving human subjects. Our laboratory is planning such a study as part of our future work.

ETHICS APPROVAL AND CONSENT TO PARTICIPATE

Not applicable.

HUMAN AND ANIMAL RIGHTS

No animals/humans were used for studies that are basis of this research.

CONSENT FOR PUBLICATION

Not applicable.

AVAILABILITY OF DATA AND MATERIALS

The image reconstruction software in MATLAB and ultrawideband data captured from these studies are available from the corresponding author, [M-ZA], upon reasonable request.

FUNDING

This work has been supported by the Malaysia Higher Education Ministry under the Prototype Research Grant Scheme, 203.PELECT.6740037.

CONFLICT OF INTEREST

The authors declare no conflict of interest, financial or otherwise.

ACKNOWLEDGEMENTS

Declared none.

REFERENCES

[1] DeSantis CE, Ma J, Gaudet MM, *et al.* Breast cancer statistics, 2019. CA Cancer J Clin 2019; 69(6): 438-51. http://dx.doi.org/10.3322/caac.21583 PMID: 31577379

[2] Bray F. Transitions in human development and the global cancer burden. World Cancer Report 2014; 4(15): 54-68.

[3] Gøtzsche PC, Jørgensen KJ. Screening for breast cancer with mammography. Cochrane Database Syst Rev 2013; 1(6): CD001877. PMID: 23737396

[4] Autier P, Boniol M. Mammography screening: A major issue in medicine. Eur J Cancer 2018; 90: 34-62. http://dx.doi.org/10.1016/j.ejca.2017.11.002 PMID: 29272783

[5] Modiri A, Goudreau S, Rahimi A, Kiasaleh K. Review of breast screening: Toward clinical realization of microwave imaging. Med Phys 2017; 44(12): e446-58. http://dx.doi.org/10.1002/mp.12611 PMID: 28976568

[6] van den Ende C, Oordt-Speets AM, Vroling H, van Agt HME. Benefits and harms of breast cancer screening with mammography in women aged 40-49 years: A systematic review. Int J Cancer 2017; 141(7): 1295-306. http://dx.doi.org/10.1002/ijc.30794 PMID: 28542784

[7] Houssami N, Nehmat H. Overdiagnosis of breast cancer in population screening: Does it make breast screening worthless? Cancer Biol Med 2017; 14(1): 1-8. http://dx.doi.org/10.20892/j.issn.2095-3941.2016.0050 PMID: 28443199

[8] Diacon AH, Pym A, Grobusch M, *et al.* The diarylquinoline TMC207 for multidrug-resistant tuberculosis. N Engl J Med 2009; 360(23): 2397-405.

[9] Fear EC, Hagness SC, Meaney PM, Okoniewski M, Stuchly MA. Enhancing breast tumor detection with near-field imaging. IEEE Microw Mag 2002; 3(1): 48-56. http://dx.doi.org/10.1109/6668.990683

[10] Fear EC, Meaney PM, Stuchly MA. Microwaves for breast cancer detection? IEEE Potentials 2003; 22(1): 12-8. http://dx.doi.org/10.1109/MP.2003.1180933

[11] Fear EC, Li X, Hagness SC, Stuchly MA. Confocal microwave imaging for breast cancer detection: Localization of tumors in three dimensions. IEEE Trans Biomed Eng 2002; 49(8): 812-22. http://dx.doi.org/10.1109/TBME.2002.800759 PMID: 12148820

[12] Xie Y, Guo B, Xu L, Li J, Stoica P. Multistatic adaptive microwave imaging for early breast cancer detection. IEEE Trans Biomed Eng 2006; 53(8): 1647-57. http://dx.doi.org/10.1109/TBME.2006.878058 PMID: 16916099

[13] Guo B, Wang Y, Li J, Stoica P, Wu R. Microwave imaging *via* adaptive beam forming methods for breast cancer detection. J Electromagn Waves Appl 2006; 20(1): 53-63. http://dx.doi.org/10.1163/156939306775777350

[14] Li X, Hagness SC. A confocal microwave imaging algorithm for breast cancer detection. IEEE Microw Wirel Compon Lett 2001; 11(3): 130-2. http://dx.doi.org/10.1109/7260.915627

[15] Li Y, Porter E, Coates M. Imaging-based classification algorithms on clinical trial data with injected tumour responses. In: 2015 9th European Conference on Antennas and Propagation (EuCAP); 2015 Apr 13-17; Lisbon, Portugal; pp. 1-5.

[16] Hagness SC, Taflove A, Bridges JE. Two-dimensional FDTD analysis of a pulsed microwave confocal system for breast cancer detection: Fixed-focus and antenna-array sensors. IEEE Trans Biomed Eng 1998; 45(12): 1470-9. http://dx.doi.org/10.1109/10.730440 PMID: 9835195

[17] Aldhaeebi MA, Alzoubi K, Almoneef TS, Bamatraf SM, Attia H, M Ramahi O. Review of microwaves techniques for breast cancer detection. Sensors (Basel) 2020; 20(8): 1-38. http://dx.doi.org/10.3390/s20082390 PMID: 32331443

[18] Elahi MA, O'Loughlin D, Lavoie BR, *et al.* Evaluation of image reconstruction algorithms for confocal microwave imaging: Application to patient data. Sensors (Basel) 2018; 18(6): E1678. http://dx.doi.org/10.3390/s18061678 PMID: 29882893

[19] Lim HB, Nhung NTT, Li EP, Thang ND. Confocal microwave imaging for breast cancer detection: Delay-multiply-and-sum image reconstruction algorithm. IEEE Trans Biomed Eng 2008; 55(6): 1697-704. http://dx.doi.org/10.1109/TBME.2008.919716 PMID: 18714833

[20] Mozaffarzadeh M, Mahloojifar A, Orooji M, Adabi S, Nasiriavanaki M. Double-stage delay multiply and sum beamforming algorithm: Application to linear-array photoacoustic imaging. IEEE Trans Biomed Eng 2018; 65(1): 31-42. http://dx.doi.org/10.1109/TBME.2017.2690959 PMID: 28391187

[21] Hollman KW, Rigby KW, O'donnell M. Coherence factor of speckle from a multi-row probe. In: 1999 IEEE Ultrasonics Symposium Proceedings International Symposium (Cat No 99CH37027); 1999 Oct 17-20; Tahoe, NV, USA; pp.1257-60. http://dx.doi.org/10.1109/ULTSYM.1999.849225

[22] Tiang SS, Hathal MS, Anwar NS, Ain MF, Abdullah MZ. Development of a compact wide-slot antenna for early stage breast cancer detection featuring circular array full-view geometry. Int J Antennas Propag 2014; 2014: 309321. http://dx.doi.org/10.1155/2014/309321

[23] Nilsen CIC, Holm S. Wiener beamforming and the coherence factor in ultrasound imaging. IEEE Trans Ultrason Ferroelectr Freq Control 2010; 57(6): 1329-46. http://dx.doi.org/10.1109/TUFFC.2010.1553 PMID: 20529709

[24] Mozumi M, Hasegawa H. Adaptive beamformer combined with phase coherence weighting applied to ultrafast ultrasound. Appl Sci (Basel) 2017; 8(2): 204-9. http://dx.doi.org/10.3390/app8020204

[25] Nilavalan R, Gbedemah A, Craddock IJ, Li X, Hagness SC. Numerical investigation of breast tumour detection using multi-static radar. Electron Lett 2003; 39(25): 8-9. http://dx.doi.org/10.1049/el:20031183

[26] Panduro MA, Reyna A, Covarrubias DH. Non-uniform concentric rings design for ultra-wideband arrays. Sensors (Basel) 2019; 19(10): 2262. http://dx.doi.org/10.3390/s19102262 PMID: 31100825

[27] Bianchi D, Genovesi S, Monorchio A. Constrained pareto optimization of wide band and steerable concentric ring arrays. IEEE Trans Antenn Propag 2012; 60(7): 3195-204. http://dx.doi.org/10.1109/TAP.2012.2196909

[28] Dietrich CB Jr. Antenna Arrays and Beamforming 2000.

[29] Camacho J, Parrilla M, Fritsch C. Phase coherence imaging. IEEE Trans Ultrason Ferroelectr Freq Control 2009; 56(5): 958-74.

[30] Hahn SL. Hilbert transforms in signal processing. Boston: Artech House 1996; Vol. 2.

[31] Shbat M, Ordaz-Salazar FC, González-Salas JS. Introductory chapter: Smart antennas and beam-formation. In: Shbat M, Ed. Antenna Arrays and Beam-formation. London: IntechOpen 2017; p. 1.
[32] Rummel S. Tumor within the breast: Does tumour site has prognostic ability? Ecancermedicalscience 2015; 2015: 9.
[33] Porter E, Fakhoury J, Oprisor R, Coates M, Popović M. Improved tissue phantoms for experimental validation of microwave breast cancer detection. In: Proceedings of the Fourth European Conference on Antennas and Propagation; 2010 Apr 12-16; Barcelona, Spain; pp. 1-5.
[34] Tiang SS, Ain MF, Abdullah MZ. Compact and wideband wide-slot antenna for microwave imaging system In: 2011 IEEE International RF & Microwave Conference; 2011 Dec 12-14; Seremban, Malaysia; pp. 63-6.
http://dx.doi.org/10.1109/RFM.2011.6168696
[35] Kwon S, Lee S. Recent advances in microwave imaging for breast cancer detection. Int J Biomed Imaging 2016; 2016: 5054912.
http://dx.doi.org/10.1155/2016/5054912 PMID: 28096808